








# Lipid droplet–size mapping in human adipose tissue using a clinical 3T system

Dominik Weidlich<sup>1</sup>  | Julius Honecker<sup>2</sup>  | Christof Boehm<sup>1</sup>  | Stefan Ruschke<sup>1</sup>  | Daniela Junker<sup>1</sup> | Anh T. Van<sup>1</sup> | Marcus R. Makowski<sup>1</sup> | Christina Holzapfel<sup>3</sup> | Melina Claussnitzer<sup>4,5,6</sup>  | Hans Hauner<sup>2,3</sup>  | Dimitrios C. Karampinos<sup>1</sup> 

<sup>1</sup>Department of Diagnostic and Interventional Radiology, School of Medicine, Technical University of Munich, Munich, Germany

<sup>2</sup>Else Kröner Fresenius Center for Nutritional Medicine, School of Life Sciences, Technical University of Munich, Munich, Germany

<sup>3</sup>Institute for Nutritional Medicine, School of Medicine, Technical University of Munich, Munich, Germany

<sup>4</sup>Broad Institute of MIT and Harvard, Cambridge, Massachusetts, USA

<sup>5</sup>Division of Gerontology, Department of Medicine, Beth Israel Deaconess Medical Center, Boston, Massachusetts, USA

<sup>6</sup>Harvard Medical School, Harvard University, Boston, Massachusetts, USA

## Correspondence

Dominik Weidlich, Department of Diagnostic and Interventional Radiology, School of Medicine, Technical University of Munich, Ismaninger Str. 22, 81675 Munich, Germany.  
Email: dominik.weidlich@tum.de

## Funding information

European Research Council, Grant/Award Number: (677661 [ProFatMRI] and 875488 [FatVirtualBiopsy]); Philips Healthcare, and the Else Kröner-Fresenius Foundation (Bad Homburg, Germany)

**Purpose:** To develop a methodology for probing lipid droplet sizes with a clinical system based on a diffusion-weighted stimulated echo–prepared turbo spin-echo sequence and to validate the methodology in water–fat emulsions and show its applicability in ex vivo adipose-tissue samples.

**Methods:** A diffusion-weighted stimulated echo–prepared preparation was combined with a single-shot turbo spin-echo readout for measurements at different b-values and diffusion times. The droplet size was estimated with an analytical expression, and three fitting approaches were compared: magnitude-based spatial averaging with voxel-wise residual minimization, complex-based spatial averaging with voxel-wise residual minimization, and complex-based spatial averaging with neighborhood-regularized residual minimization. Simulations were performed to characterize the fitting residual landscape and the approaches' noise performance. The applicability was assessed in oil-in-water emulsions in comparison with laser deflection and in ten human white adipose tissue samples in comparison with histology.

**Results:** The fitting residual landscape showed a minimum valley with increasing extent as the droplet size increased. In phantoms, a very good agreement of the mean droplet size was observed between the diffusion-weighted MRI-based and the laser deflection measurements, showing the best performance with complex-based spatial averaging with neighborhood-regularized residual minimization processing ( $R^2/P$ : 0.971/0.014). In the human adipose-tissue samples, complex-based spatial averaging with neighborhood-regularized residual minimization processing showed a significant correlation ( $R^2/P$ : 0.531/0.017) compared with histology.

This is an open access article under the terms of the Creative Commons Attribution-NonCommercial License, which permits use, distribution and reproduction in any medium, provided the original work is properly cited and is not used for commercial purposes.

© 2021 The Authors. *Magnetic Resonance in Medicine* published by Wiley Periodicals LLC on behalf of International Society for Magnetic Resonance in Medicine.

**Conclusion:** The proposed acquisition and parameter-estimation methodology was able to probe restricted diffusion effects in lipid droplets. The methodology was validated using phantoms, and its feasibility in measuring an apparent lipid droplet size was demonstrated *ex vivo* in white adipose tissue.

**KEYWORDS**

adipocyte diameter, adipose tissue microstructure, DW-TSE, fat diffusion, lipid droplet

## 1 | INTRODUCTION

The assessment of lipid droplet size is important to study adipose-tissue (AT) remodeling in both health and metabolic dysfunction. In white AT (WAT), adipocytes contain unilocular lipid droplets with a diameter between 50  $\mu\text{m}$  and 150  $\mu\text{m}$  and a thin surrounding cytoplasm. Thereby, the lipid droplet size is typically considered synonymous for the adipocyte size. With the onset of obesity, an increase in adipocyte size in subcutaneous and visceral WAT can be observed in adults.<sup>1,2</sup> WAT adipocyte size is known to be associated with comorbidities of obesity such as type 2 diabetes, dyslipidemia, and cardiometabolic risk.<sup>3</sup> Therefore, adipocyte size assessment is highly desirable to identify the patient's risk to develop obesity-related medical conditions. Currently, however, the measurement of adipocyte size requires invasive biopsy procedures.<sup>4</sup>

Diffusion-weighted (DW) MR is a powerful approach for the noninvasive probing of tissue microstructure. The reduction of the ADC with increasing diffusion times due to diffusion-restriction effects has been applied extensively to estimate cell size in water-containing tissues.<sup>5</sup> Measuring lipid-diffusion properties remains challenging, as fat has a diffusion coefficient approximately two orders of magnitude lower than water.<sup>6,7</sup> The low fat diffusivity imposes the requirement for high *b*-values and long diffusion times to measure diffusion-restriction effects, inducing further technical challenges related to eddy currents<sup>8</sup> and increased motion sensitivity.<sup>9,10</sup> However, even when using high *b*-values and long diffusion times, the extraction of lipid droplet size from DW measurements requires high SNR,<sup>11</sup> especially due to small diffusion-restriction effects when probing large lipid droplet sizes in human WAT.

Diffusion-weighted MRS (DW-MRS) is a versatile tool that allows to measure diffusion properties of metabolites other than water<sup>12,13</sup> and has recently been applied to study lipid diffusion. Specifically, high *b*-value single-voxel DW-MRS techniques have been applied to study myocellular lipid diffusion,<sup>14</sup> to quantify the intramyocellular lipid droplet size<sup>15</sup> and to study murine brown adipocytes.<sup>16</sup> However, most of the existing lipid DW-MRS work has been performed *ex vivo*, investigating small lipid droplets (below 10  $\mu\text{m}$ ) using the gradient hardware of preclinical systems. Only recently, the feasibility

of using DW-MRS was reported for the *in vivo* probing of lipid droplet size in human bone marrow adipocytes on a clinical system, which represents a milestone toward probing the lipid droplet size in larger WAT adipocytes.<sup>11</sup>

Single-voxel DW-MRS allows high SNR but is associated with important limitations when aiming at clinical translation of the lipid droplet size measurement: Due to the large voxel size, DW-MRS is sensitive to motion-induced intravoxel dephasing effects, which results in quantification errors. Acquiring data with smaller voxel size would mitigate this effect and is an important step toward *in vivo* applicability. Neighborhood information could also lead to a more robust lipid droplet size fitting, but with single-voxel MRS no neighborhood information is encoded. Acquiring spatially resolved data would allow regularized parameter fitting in the lipid droplet size estimation.

Therefore, a lipid DWI technique is desirable, which allows the acquisition of lipid signals at high *b*-values and long diffusion times to at least partly overcome the aforementioned limitations of lipid single-voxel DW-MRS. Lipid DWI will not only be less sensitive to motion/vibration effects and has the possibility to consider the voxel neighborhood in the fitting process, but potentially also allows the extraction of spatially resolved lipid droplet size maps. Previous work aiming at lipid DWI have been based on DW spin-echo single-shot EPI.<sup>7</sup> However, spin echo-based DW suffers from lower SNR when using long diffusion times, whereas EPI readouts are highly sensitive to off-resonance effects (including different chemical shift artifacts for the different fat peaks).<sup>17</sup> Instead, a stimulated echo-based (STE) preparation may allow to probe diffusion restriction effects at long diffusion times, and a single-shot turbo spin-echo (TSE) readout could reduce the sensitivity to chemical shift artifacts.<sup>18</sup>

Therefore, the purpose of the present work was to (1) develop a DW-STE-prepared single-shot TSE sequence for measuring lipid diffusion using a clinical 3T system, (2) develop the processing for lipid droplet size mapping, (3) validate the methodology in water-fat emulsions by comparing the MR results with laser deflection measurements (methodology to measure lipid particle-size distributions<sup>19</sup>) and (4) to investigate the methodology in *ex vivo* human AT samples by comparing the MR results with histology.

## 2 | METHODS

### 2.1 | Pulse sequence

A nonselective 3D DW-STE preparation consisting of four  $90^\circ$  Malcom-Levitt RF pulses<sup>20</sup> and monopolar diffusion gradients combined with a single-shot 2D TSE readout (Figure 1) was developed. To eliminate eddy current-induced and motion-induced phase errors, magnitude-stabilizing gradients following Alsop's method<sup>18</sup> were introduced in preparation and readout.<sup>21</sup> The b-value was adjusted by changing the diffusion gradient strength. The diffusion time was changed by varying the mixing time (TM) of the preparation module. The DW-STE preparation was designed to allow the strong DW necessary to investigate lipid diffusion, while offering the possibility to increase the diffusion time with minor signal attenuation. The influence of residual water signal was reduced by only acquiring DW signals at b-values above  $5000 \text{ mm}^2/\text{s}$  and by a frequency selectivity of the preparation module that additionally attenuates the water signal. The preparation module has a bandwidth of approximately  $\pm 400 \text{ Hz}$ , and the Malcom-Levitt RF pulses were used to ensure a decent robustness against  $B_1$  inhomogeneities with moderate specific absorption rate penalty (Supporting Information Figure S1). The center frequency was set manually to the main fat peak in all subsequent experiments. The maximum b-value and diffusion time were empirically selected to be as large as possible, while simultaneously ensuring a sufficient SNR in the measurement protocols listed subsequently.

### 2.2 | Reconstruction and preprocessing of DW images

The obtained k-space data were low-pass-filtered using a Hanning window filter. Different sizes of the filter were

empirically tested and the results were inspected visually. A filter size of half of the k-space window was selected and used for the subsequent processing because it provided a robust estimation of the low-resolution phase term. The low-resolution phase term was extracted and subsequently subtracted from the corresponding full-resolution DW image.<sup>22</sup> Afterward, the effective SNR ( $\text{SNR}_{\text{effective}}$ ) was increased by spatially averaging the DW image under the assumption that the tissue heterogeneity is small. Spatial averaging was performed by taking the signal's mean within a square with a certain voxels edge length. The value of  $\text{SNR}_{\text{effective}}$  was equal to  $\sqrt{N} \cdot \text{SNR}_0$ , where  $N$  is equal to the number of voxels that are averaged and  $\text{SNR}_0$  is the SNR of a single voxel. The 2D spatial averaging was either performed on the magnitude or the complex DW images separately for each diffusion time, b-value, and average.

### 2.3 | Lipid droplet size estimation

The lipid droplet size can be estimated based on DW signals, previously measured by DW-MRS<sup>11</sup> with the corresponding cost function  $C$ :

$$C = \left\| S_0 \cdot S_{\text{Murday\&Cotts}}(d, D) \cdot \exp\left(-\frac{TM}{T_1}\right) - S_{\text{exp}} \right\|^2 \quad (1)$$

where  $S_0$  is the signal without DW;  $S_{\text{Murday\&Cotts}}$  is the theoretical DW signal,<sup>23</sup>  $d$  is the restricting spherical barrier diameter,  $D$  is the free diffusion constant,  $TM$  is the DW-STE preparation's mixing time,  $T_1$  is the longitudinal relaxation constant, and  $S_{\text{exp}}$  is the measured signal.

The obtained DW images can be used to fit the lipid droplet size spatially resolved by minimizing the cost function  $C$  voxel-wise. Fitting was performed using a nonnegative least-squares fitting using the trust-region-reflective algorithm by *MATLAB*

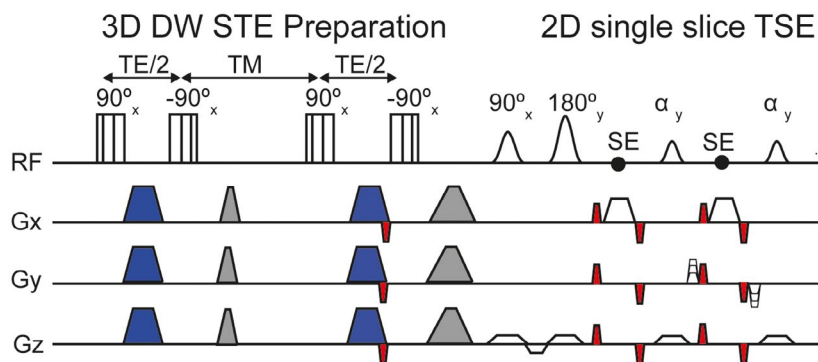


**FIGURE 1** Sequence diagram of the proposed diffusion-weighted (DW) stimulated echo-based (STE)-prepared single-shot 2D turbo spin echo (TSE). The DW-STE magnetization preparation consists of four composite  $90^\circ$  Malcom-Levitt RF pulses and monopolar diffusion-sensitizing gradients (blue). To eliminate eddy current-induced and motion-induced phase errors, an additional pair of dephasing/rephasing gradients (indicated in red), denoted as magnitude stabilizers, are introduced before the last tip-up pulse. Additional, magnitude stabilizers are performed immediately before and after every spin-echo formation (also indicated in red). The spoiler gradients within the magnetization preparation are indicated in gray. Abbreviations: SE, spin echo; TE, echo time; TM, mixing time

(MathWorks, Natick, MA). To avoid local minima at each voxel, the fitting was performed with multiple initial starting value pairs ( $i$ ) for  $d$  and  $D$ . The residual  $res_i(r)$  and the estimated parameters  $d_i(r)$ ,  $D_i(r)$ ,  $T_{1_i}(r)$ ,  $S_{0_i}(r)$  were recorded for each initial starting value pair  $i$  and voxel location  $r$ . The initial starting values were selected to be close to the expected parameter values but also covering a large range. Therefore, the initial starting values for phantom fitting were  $d = 4\text{--}28\ \mu\text{m}$  in  $4\text{-}\mu\text{m}$  steps,  $D = 6 \times 10^{-6}\ \text{mm}^2/\text{s}$  to  $10 \times 10^{-6}\ \text{mm}^2/\text{s}$  in  $0.5 \times 10^{-6}\ \text{mm}^2/\text{s}$  steps, and  $T_1 = 300\ \text{ms}$ . The value of  $S_0$  was estimated based on the other initial starting values and the maximum value of the noisy signal. For the AT samples case, the initial starting values for the fitting were  $d = 20\text{--}80\ \mu\text{m}$  in  $10\text{-}\mu\text{m}$  steps,  $D = 6 \times 10^{-6}\ \text{mm}^2/\text{s}$  to  $10 \times 10^{-6}\ \text{mm}^2/\text{s}$  in  $0.5 \times 10^{-6}\ \text{mm}^2/\text{s}$  steps, and  $T_1$  and  $S_0$  were the same as in the phantom case.

The final parameters were estimated by finding either a voxel-wise minimum or a neighborhood-regularized global minimum. Figure 2 shows an overview of the processing pipeline. Combined with the possibility of performing a magnitude-based (resulting in the residuals  $res_{Mbi}[r]$ ) or complex-based (resulting in the residuals  $res_{Cbi}[r]$ ) averaging before the parameter estimation, different processing schemes can be distinguished.

Specifically, three different ways of processing were compared: magnitude-based spatial averaging with voxel-wise residual minimization (MbV, red color in figures), complex-based spatial averaging with voxel-wise residual minimization (CbV, blue color in figures), and complex-based spatial averaging with neighborhood-regularized residual minimization (CbR, green color in figures). In Figure 2, only the

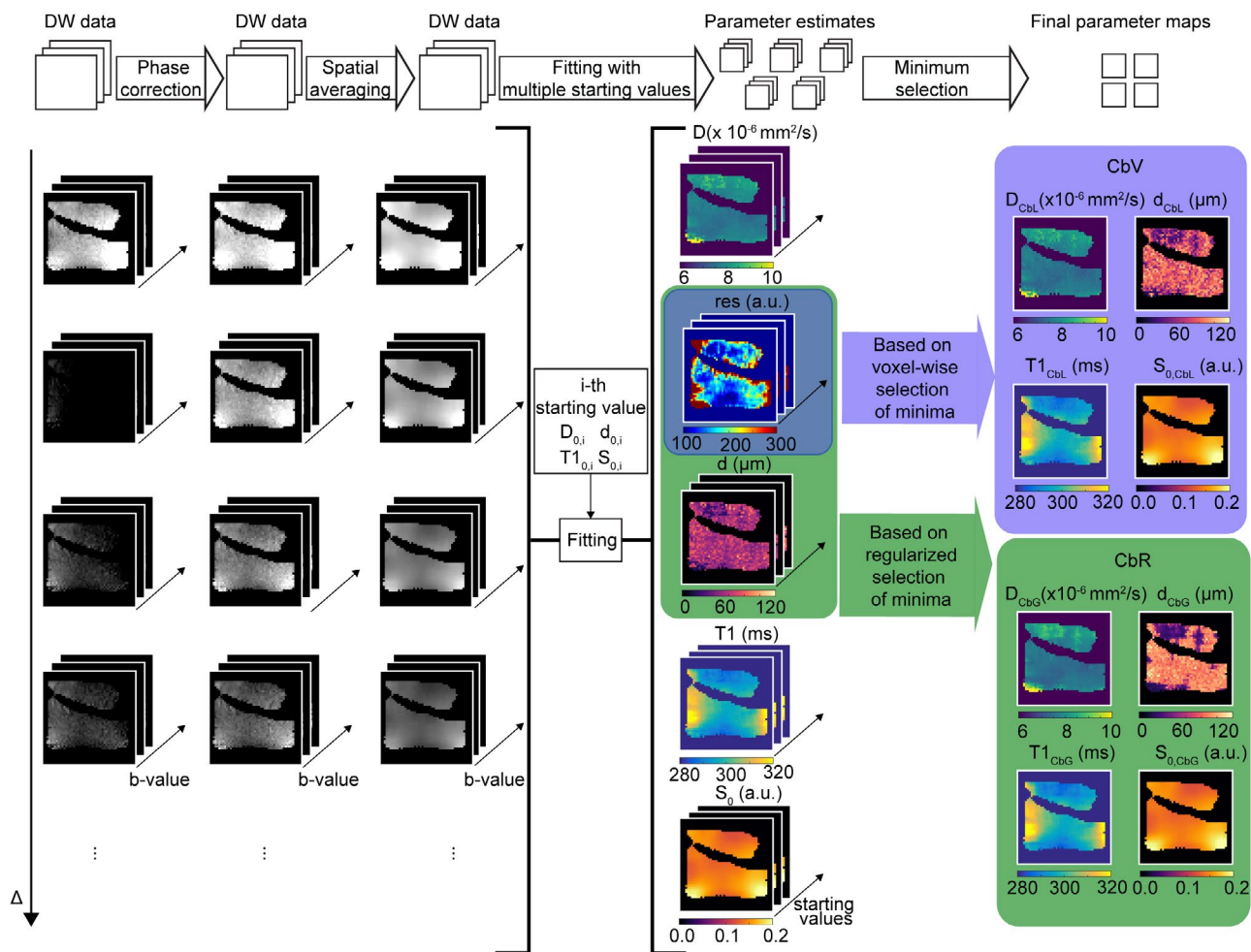


**FIGURE 2** Overview of fitting process is shown in one adipose-tissue (AT) sample. Data are acquired with different diffusion times ( $\Delta$ , rows) and diffusion weightings (b-value, diagonal dimension). First, the complex data are phase-corrected and then spatially averaged to increase SNR. All data are pooled, and a voxel-wise fitting is performed with different initial starting values. The fitting process leads to different estimates for the parameter maps. The final parameter maps can be obtained from the estimates in two different ways. Taking the voxel-wise estimate with lowest residual leads to the magnitude-based spatial averaging with voxel-wise residual minimization (MbV) processing (not shown) when using magnitude data or CbV processing (blue) using complex data. Using the complex data and additionally imposing a spatially slowly varying lipid droplet size (represented by its diameter) leads to the CbR processing (green). Abbreviations: CbR, complex-based spatial averaging with neighborhood-regularized residual minimization; CbV, complex-based spatial averaging with voxel-wise residual minimization

CbV and the CbR processing are shown because the MbV processing is identical to CbV besides the performed spatial averaging.

### 2.3.1 | Magnitude-based spatial averaging with voxel-wise residual minimization

Spatial averaging was first performed on the magnitude DW images. Fitting was then performed voxel-wise for multiple initial starting values, and an analysis of the residuals was performed at each voxel location  $r$  as follows:

$$[d_{MbV}(r), D_{MbV}(r), T1_{MbV}(r), S_{0,MbV}(r)] = \arg \min_{d(r), D(r), T1(r), S_0(r)} res_{Mb}(r) \quad (2)$$

### 2.3.2 | Complex-based spatial averaging with voxel-wise residual minimization

Spatial averaging was first performed on the complex DW images. Fitting was then performed voxel-wise for multiple initial starting values, and an analysis of the residuals was performed at each spatial location  $r$  as follows:

$$[d_{CbV}(r), D_{CbV}(r), T1_{CbV}(r), S_{0,CbV}(r)] = \arg \min_{d(r), D(r), T1(r), S_0(r)} res_{Cb}(r) \quad (3)$$

### 2.3.3 | Complex-based spatial averaging with neighborhood-regularized residual minimization

Spatial averaging was first performed on the complex DW images, and the fitting was performed voxel-wise with different initial starting values. A global analysis was then performed, imposing a small spatial lipid droplet-size variation. Therefore, the fitted parameters in each voxel were selected not only based on the local voxel residual but also by penalizing large diameter variations in the Von Neumann neighborhood (representing the four adjacent voxels) of the voxel ( $N[r]$ ). A regularized global cost function similar to Cui et al<sup>24</sup> and Boehm et al<sup>25</sup> was used, in which  $res_{Cb}(r)$  replaced the data-consistency term, and the regularization term was the estimated diameter's variation in the voxel's neighborhood. The minimization problem was solved with a graph-cut algorithm using a graph construction with convex priors that allows for unequally sampled space<sup>26</sup> in the diameter dimension:

$$[d_{CbR}(r), D_{CbR}(r), T1_{CbR}(r), S_{0,CbR}(r)] = \arg \min_{d(r), D(r), T1(r), S_0(r)} \sum_r res_{Cb}(r) + \lambda c. \sum_{s \in N(r)} \|d(r) - d(s)\| \quad (4)$$

The regularization parameter  $\lambda$  was chosen following the discrepancy principle and was set to 0.1. The discrepancy principle states that the regularization term should be similar to the noise floor.<sup>27</sup> The used regularization term was approximately 10% of the data consistency term.

## 2.4 | Phantom manufacturing

Four high-fat water-fat phantoms (oil-in-water emulsions) resembling in vivo AT lipid content were produced. Each phantom contained 800 mL sunflower oil (ARO), 200 mL water, 20 mL Tween 80 (Sigma-Aldrich, Taufkirchen, Germany), and 1 g of sodium benzoate (Roth, Karlsruhe, Germany). Emulsification was carried out with a colloid mill (IKA Labor-Pilot 2000/4; IKA-Werke, Staufen, Germany) at 5000/6000/9000/12 000 revolutions per minute to obtain different oil droplet sizes (standardized emulsification process<sup>28</sup>). The particle size was measured by dynamic light scattering using a particle-sizing instrument (Mastersizer 2000; Malvern Instruments, Worcestershire, United Kingdom). Samples were diluted with 0.5% sodium dodecyl sulfate (Serva; Heidelberg, Germany) solution (1:10, vol/vol) to separate agglomerates and measure single lipid droplets.<sup>19</sup> From the particle-size distributions, mean diameters were extracted.

## 2.5 | Adipose tissue sampling

Ten abdominal subcutaneous AT samples were obtained from patients undergoing abdominoplasty after severe weight loss. The study was approved by the local ethics commission, and written consent was obtained. Small pieces from the AT samples were fixed in formalin for histological processing. After slicing and staining with hematoxylin and eosin, images were taken in high-definition range at  $\times 200$  magnification (VHX-6000I Keyence, Osaka, Japan). Adipocyte area determination was carried out using the proprietary microscope image analysis software (VHX-6000; Keyence) by automatically identifying round objects within the histology slice and obtaining the object's area. A lower ( $200 \mu\text{m}^2$ ) and upper size limit ( $16\ 000 \mu\text{m}^2$ ) were used to remove objects typically representing artifacts, cell debris, or ruptured adipocytes. Each image was manually inspected after automated identification. Adipocyte diameter was calculated assuming a spherical shape.<sup>4</sup>

## 2.6 | Numerical analysis of fitting residual landscape

To investigate the residual landscape of the fitting, the difference of the signal decay curves relative to selected reference

signals was calculated based on the cost function  $C$  ( $T_1 = 300$  ms and  $S_0 = 100$  were assumed while varying the free diffusion constant and diameter). The following measurement scenarios were distinguished due to different scan protocols.

In the phantom case, the protocol included 50 pairs of b-value and TM, with b-values of 5000 to 50 000 s/mm<sup>2</sup> in 5000-s/mm<sup>2</sup> steps and TM of 200-400 ms in 50-ms steps. The reference signals were simulated for droplet diameters of 4  $\mu$ m and 12  $\mu$ m and for a free diffusion constant of  $8 \times 10^{-6}$  mm<sup>2</sup>/s. The difference relative to these two reference signals was calculated for a range of combinations of droplet diameter (2-30  $\mu$ m) and free diffusion constant ( $[7.5-8.5] \times 10^{-6}$  mm<sup>2</sup>/s).

In the AT sample case, the protocol included 110 pairs of b-value and TM, with b-values of 5000 to 50 000 s/mm<sup>2</sup> in 5000-s/mm<sup>2</sup> steps and TM of 200-700 ms in 50-ms steps. The reference signals were simulated for droplet diameters of 50  $\mu$ m and 60  $\mu$ m and for a free diffusion constant of  $8 \times 10^{-6}$  mm<sup>2</sup>/s. The difference relative to these two reference signals was calculated for a range of combinations of droplet diameter (20-120  $\mu$ m) and free diffusion constant ( $[7.5-8.5] \times 10^{-6}$  mm<sup>2</sup>/s).

## 2.7 | Noise performance analysis

To characterize the three processing approaches, a noise simulation was performed using as ground truth the signal from the fitting residual landscape numerical analysis (droplet diameter in phantom case [12  $\mu$ m] and droplet diameter in AT sample [60  $\mu$ m]). Gaussian noise was added to the real and imaginary part of the complex signal to achieve a SNR<sub>0</sub> (defined for the first b-value and diffusion time). The value of SNR<sub>0</sub> was selected as the approximate lower SNR limit from the subsequent experimental scans. Spatial averaging was simulated by averaging the magnitude or complex data within a square window of 1-11 voxels edge length. Therefore, noise was first added over groups of  $1^2/2^2/3^2/4^2/5^2/6^2/7^2/8^2/9^2/10^2/11^2$  voxels, and the signals were averaged in a second step that led to variable SNR<sub>effective</sub>. At each size of the averaging window, the spatially averaged signal was then used to perform the fitting with multiple starting values. The noisy signal generation and averaging was repeated 1089 (corresponding to a 33  $\times$  33 voxel 2D slice) times, resulting in 1089 noisy samples at each SNR level (depending on the size of the averaging window), and statistics were extracted for the MbV and CbV processing.

To evaluate the performance of the regularized fitting, the 1089 noise samples at each SNR level were rearranged to form a 2D slice that was processed with the CbR processing. In the phantom case, SNR<sub>0</sub> was assumed to be 75, and in the AT sample case, SNR<sub>0</sub> was assumed to be 50.

## 2.8 | Phantom measurements and analysis

Magnetic resonance scanning of the emulsion phantoms and coconut oil was performed on a 3T system (Ingenia Elition; Philips, Best, Netherlands) using an eight-channel wrist coil with the following parameters: FOV = 90  $\times$  90 mm<sup>2</sup>, acquisition voxel size = 1.4  $\times$  2.5  $\times$  10 mm<sup>3</sup>, reconstruction voxel size = 1.4  $\times$  1.4  $\times$  10 mm<sup>3</sup>, TSE factor = 36, TR/TE/TE<sub>prep</sub> = 2000/23/61 ms, five averages, 50 pairs of b-value and TM with b-values = 5000 to 50 000 s/mm<sup>2</sup> in 5000-s/mm<sup>2</sup> steps and TM = 200/250/300/350/400 ms, scan time = 8:30 minutes. To minimize vibration artifacts induced by the strong diffusion gradients, a wooden support table was used.<sup>10</sup>

Neighboring voxels (3  $\times$  3) were averaged to increase SNR<sub>effective</sub>, leading to an effective voxel size of 4.2  $\times$  4.2  $\times$  10 mm<sup>3</sup>. The lipid droplet-size fitting was performed with the initial starting values described in the noise simulations. Each average was treated as a separate b-value/TM measurement pair. The SNR was calculated as the ratio between the mean and the SD of the magnitude images across acquired averages for the first diffusion time and b-value.

## 2.9 | Ex vivo AT sample measurements and analysis

The approximately 10  $\times$  10  $\times$  5 cm<sup>3</sup> AT samples fixed in formalin were scanned using an eight-channel extremity coil with the following parameters: FOV = 120  $\times$  120 mm<sup>2</sup>, acquisition and reconstruction voxel size = 1.9  $\times$  1.9  $\times$  8 mm<sup>3</sup>, TSE factor = 64, TR/TE/TE<sub>prep</sub> = 2000/18.5/62 ms, four averages, 110 pairs of TM and b-value with b-values = 5000 to 50,000 s/mm<sup>2</sup> in 5000-s/mm<sup>2</sup> steps and TM = 200-700 ms in 50-ms steps, and scan time = 14:56 minutes. To minimize vibration artifacts, a wooden support table was used<sup>10</sup> and the ramps of the diffusion gradient were reduced. Additionally, a proton density fat fraction map was acquired with a 3D multi-echo gradient-echo sequence using bipolar gradient readout with FOV = 100  $\times$  100  $\times$  65 mm<sup>3</sup>, voxel size = 1.3  $\times$  1.3  $\times$  1.3 mm<sup>3</sup>, TR/TE1/ $\Delta$ TE = 15/1.4/1.1 ms, flip angle = 5°, and six acquired echoes. The vendor's fat quantification routine included a phase error correction and a complex-based water-fat decomposition using a precalibrated fat spectrum with a single T<sub>2</sub>\* correction.<sup>29</sup>

A neighborhood of 6  $\times$  6 voxels was averaged to increase SNR, resulting in an effective voxel size of 11.4  $\times$  11.4  $\times$  8 mm<sup>3</sup>. Each average was treated as a separate b-value/TM measurement pair. Voxel-wise SNR was calculated as the ratio between the mean magnitude signal at the first diffusion time and b-value and the SD of an additional noise scan acquired without RF and gradient power.

Given that the influence of certain tissue properties (like particle-size distribution) on the measurement of the MRI-based mean lipid droplet size is still unknown in the ex vivo AT samples, the term “apparent lipid droplet size” was used in the context of the AT study.

### 3 | RESULTS

#### 3.1 | Numerical analysis of fitting residual landscape

Figure 3 shows the signal fitting landscape for both measurement scenarios with their respective reference droplet diameters. For the diameter of 4  $\mu\text{m}$  in the phantom case, a distinct global minimum in the diameter dimension at the reference droplet diameter was observed with different free diffusion constants yielding very similar signal decay curves. With increasing diameter, the minimum residual valley got broader and more curved. Diameters smaller than the reference diameter with a free diffusion constant larger than the reference as well as diameters larger than the reference diameter with free diffusion constants smaller than the reference can have similar DW signal curves. Within the observed minimum residual valley, the differences between the signal decay curves were small, indicating a small gradient of the fitting’s cost function. In the AT case, the minimum residual valley got distinctively broader, and the range of diameter and free diffusion constant combinations resulting in small residuals increased.

#### 3.2 | Noise performance analysis

Figure 4 shows the results from the noise analysis for the phantom case. The 2D histograms of the estimated diffusion constant and droplet diameter yielded a similarly shaped

minimum valley, as in Figure 3. The broadness of the diameter and free diffusion constant distribution was reduced at higher  $\text{SNR}_{\text{effective}}$ . A noticeable bias of the mean diameter was only observed for the initial  $\text{SNR}_0$  (without averaging) for MbV (22.2% overestimation), CbV (22.2% overestimation), and CbR (17.1% overestimation). With increasing  $\text{SNR}_{\text{effective}}$ , the mean diameter and free diffusion constant approached the true value, and the associated SDs were decreasing. For CbR, the estimated parameters followed the same trend, but the SD at low  $\text{SNR}_{\text{effective}}$  was reduced compared with MbV and CbV.

In general, the noise analysis for the AT sample case (Figure 5) was comparable to the phantom case, but a higher variability in the estimated parameters and differences between the proposed methods were visible. The 2D histogram showed a broad distribution for the droplet diameter and free diffusion constant estimates for all processing approaches. When the  $\text{SNR}_{\text{effective}}$  was low, even two distinct peaks in the diameter estimation were visible in the MbV and CbV case. With increasing  $\text{SNR}_{\text{effective}}$ , these two peaks tended to merge into one. The SD in the diameter estimation appeared similar with voxel-wise estimations (MbV and CbV), whereas it was reduced with CbR. At high  $\text{SNR}_{\text{effective}}$ , quantification biases were still observed. At an  $\text{SNR}_{\text{effective}}$  of 500, the deviation from the true value was  $-10.6\%$  (MbV),  $3.9\%$  (CbV), and  $1.7\%$  (CbR).

#### 3.3 | Phantom experimental results

Supporting Information Figure S2 shows the DW signal decay for each phantom. The mono-exponential diffusion signal decay curve at each diffusion time was visible for the water-fat emulsion phantoms as well as coconut oil. The measured ADC of the coconut oil was not dependent on the diffusion time indicating free diffusion.

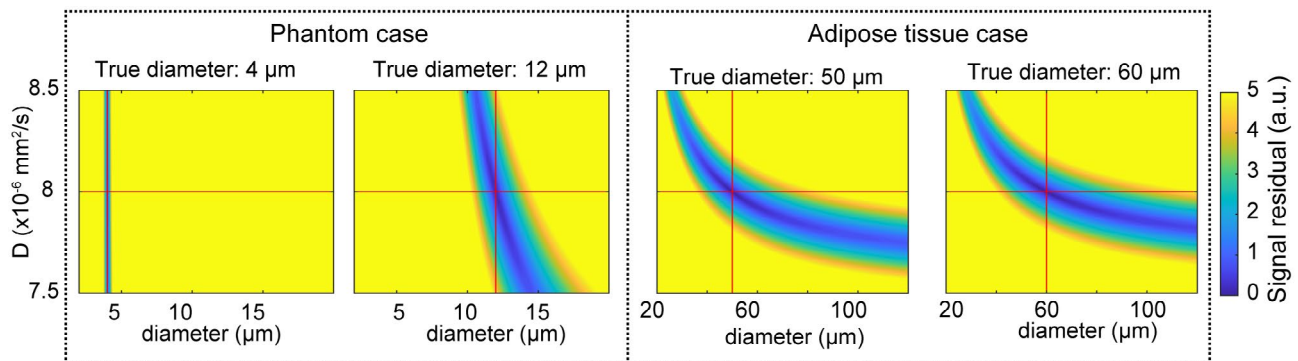


**FIGURE 3** Simulated parameter landscape of the fitting process. The differences in the signal decay curves relative to their respective selected signal (reference signal indicated with red cross) were calculated based on Equation 1. The columns show different selected diameters with the same free diffusion constant. The first two columns represent the phantom case, whereas the third and fourth columns represent the AT sample case. With increasing diameter, the minimum valleys get visually broader, indicating a decreasing gradient of the optimization function. Please note the different ranges on the x-axis (diameter dimension)

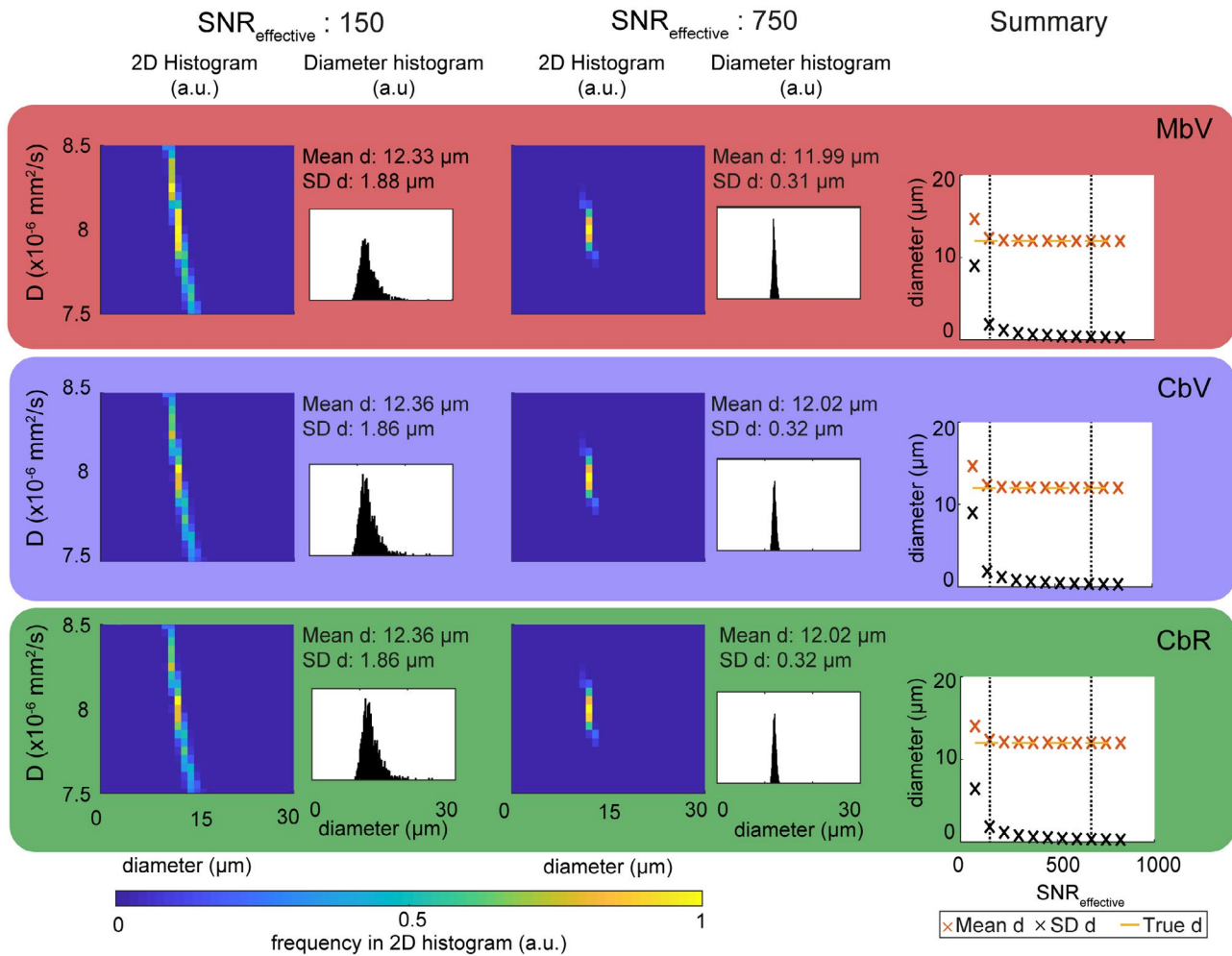


**FIGURE 4** Noise performance of the lipid droplet–size estimation in the phantom case (true diameter = 12  $\mu\text{m}$ ). The 2D histogram for diameter and diffusion constant estimates as well as a diameter histogram are shown. At low SNR, diffusion constant and diameter estimates closely reassembling the minimum valley shown in Figure 3 can be observed. The MbV and CbV processing yield very similar results. At low SNR, both measurements tend to overestimate the true diameter with an increasing SD. With increasing effective SNR, the mean diameter approaches the true value, and the SD in the estimation decreases. The CbR processing follows the trend of the CbV; however, the SD at different SNR levels is reduced. At an effective SNR ( $\text{SNR}_{\text{effective}}$ ) of 750, the bias of all methods is below 1%

Figure 6 shows the obtained phantom diameter maps. The two voxel-wise residual minimizations (MbV and CbV) resulted in nearly identical droplet diameter maps with certain regions showing local spatial heterogeneity. A trend toward larger lipid droplet sizes was observed for decreasing stirring frequency. When compared with the voxel-wise fitting, the CbR processing showed reduced spatial heterogeneity in the droplet diameter map. The free diffusion constant maps were similar in all phantoms.

Figure 7 plots the correlation of the MR-based results against the reference measurement laser deflection. The droplet diameter results from the MbV and CbV were very similar; therefore, only the CbV results were shown. In all cases, the DW-MRI results agreed well with the validation measurement ( $R^2 > 0.95$  and  $P < 5\%$ ). When the lipid droplet–size fitting was performed with CbV, the linear fit deviated from the identity line (slope/offset = 1.37/–2.52

$\mu\text{m}$ ). When CbR was used, the linear fit again approached the identity line (slope/offset = 1.13/–0.71  $\mu\text{m}$ ), and the SD of the lipid droplet–size estimation was reduced.

### 3.4 | Ex vivo AT sample experimental results

Figure 8 depicts the results from two AT samples. AT sample 1 showed smaller adipocyte sizes in histology, higher proton density fat fraction map heterogeneity, and a lower overall SNR (mean SNR of 55 compared with 78 in sample 2 [not shown]). In AT sample 1, smaller apparent lipid droplet sizes were observed with MbV compared with the other methods. The apparent diameter distribution with CbV showed two distinct peaks. With CbR, outliers were reduced in the apparent diameter map, and the height of



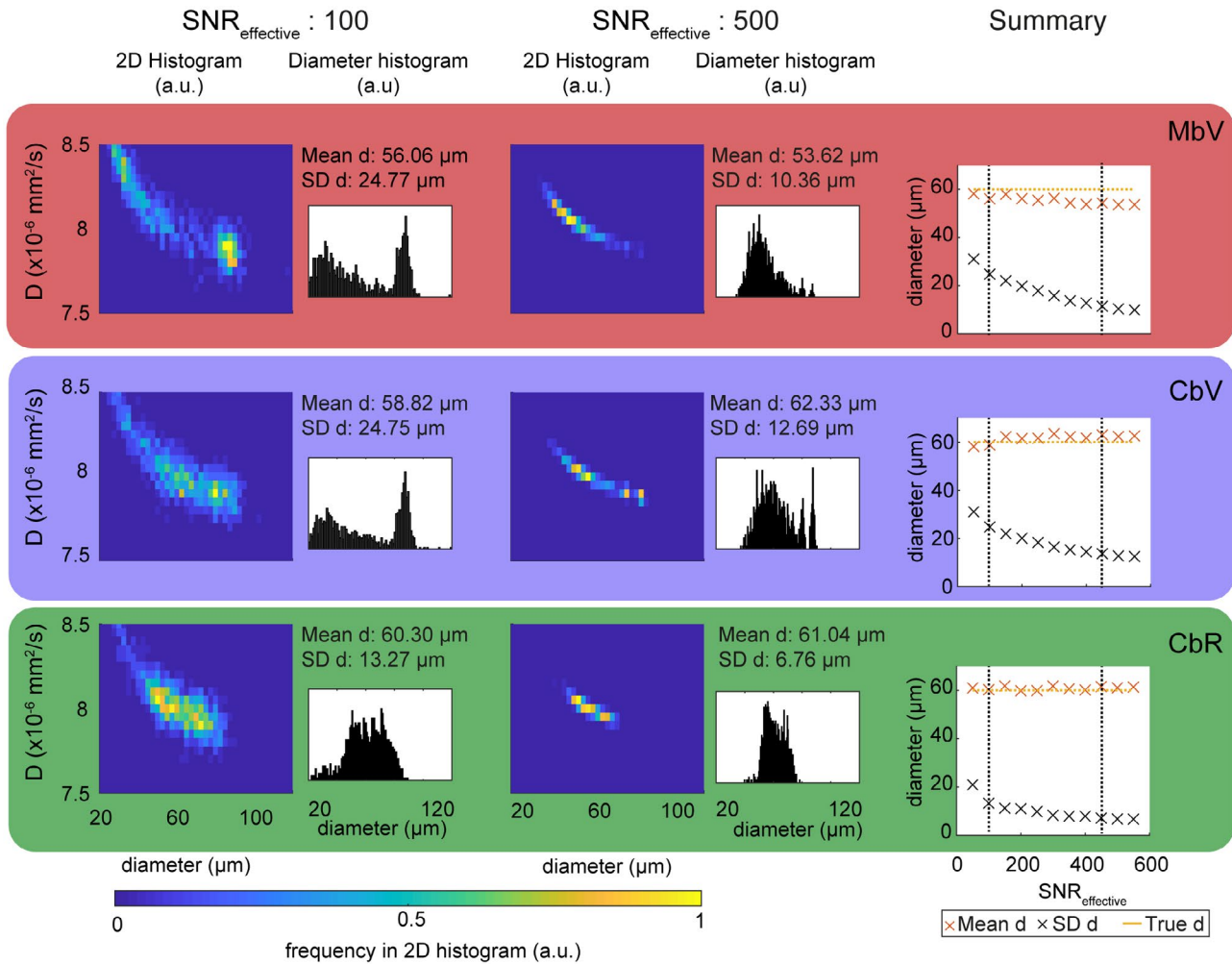


**FIGURE 5** Noise performance of the lipid droplet–size estimation in the AT sample case (true diameter = 60 μm). In the 2D histogram, a rather broad distribution for the droplet diameter and free diffusion constant estimates can be observed. The broadness and the SD in the mean diameter estimation decrease with increasing SNR. The distributions of the results obtained by MbV and CbV appear similar, whereas the broadness is reduced with CbR. At high SNR<sub>effective</sub> (by spatial averaging), quantification biases can be observed. At a SNR<sub>effective</sub> of 500, the deviation from the true diameter is –10.6% (MbV), 3.9% (CbV), and 1.7% (CbR)

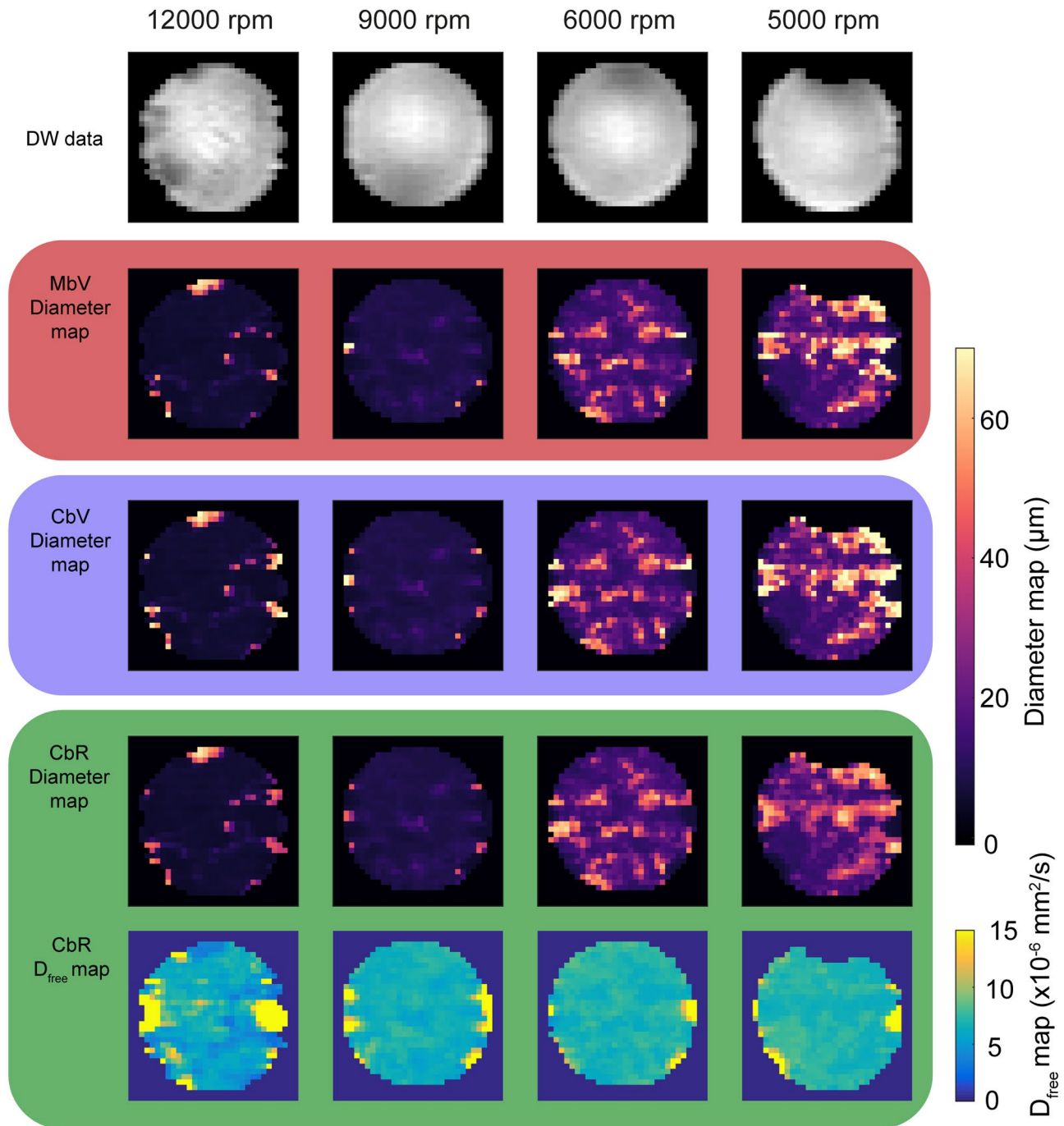
the peak at larger apparent lipid droplets was decreased. In AT sample 2, larger apparent lipid droplet sizes and a better agreement among the three processing methods was observed. The apparent diameter map obtained by MbV showed a relatively large fraction of voxels with small apparent diameter. This fraction decreased when the apparent droplet diameter map was obtained by CbV, and even further when CbR was used. The free diffusion constant maps obtained by CbR showed similar values in both samples. The obtained free diffusion constants for all phantoms and AT samples are listed in the Supporting Information (including a discussion of their agreement with literature values).

Figure 9 summarizes the results from the AT sample study, showing the mean apparent droplet size estimation obtained by the CbR processing in comparison with histology. The depicted SD for the MR-based measurement reflects the broadness of the estimated voxel-wise apparent lipid droplet

size within the acquired 2D slice. The MR-based results and the histology measurements correlated significantly ( $R^2/P$ : 0.531/0.017). The CbV processing showed a similar trend as CbR, and the MbV processing resulted in an underestimation of the mean apparent lipid droplet size and no significant correlation with histology (both processing methods not shown in Figure 9).

## 4 | DISCUSSION

The present study proposes a methodology to noninvasively measure lipid droplet size based on a novel lipid DWI acquisition and lipid droplet–size parameter-estimation approaches. The work shows that it is feasible to measure large lipid droplet size in phantoms and to provide an apparent estimate of lipid droplet sizes in ex vivo human specimens using a clinical 3T system.



**FIGURE 6** Diffusion-weighted imaging data (first row) and corresponding diameter maps for the water–fat emulsion phantoms with the three examined processing approaches. For the CbR processing, the free diffusion constant map is also shown (last row). All processing approaches show an increasing lipid droplet size with decreasing rotation frequency of the colloid mill. Local overestimations of the measured lipid droplet size are visible with the processing approaches with a voxel-wise residual minimization (MbV and CbV), but are reduced with CbR processing. The free diffusion constant is rather similar in all investigated phantoms. Abbreviation: rpm, revolutions per minute

Regarding lipid DWI acquisition, a high  $b$ -value DW-STE single-shot TSE acquisition was developed. To measure lipid diffusion in water–fat mixtures, the interference with water signals needs to be reduced. The proposed sequence is tailored to this need, because the used STE preparation has a frequency selectivity with the resonance frequency centered on the main fat peak. In addition, only images with very high

$b$ -values ( $\geq 5,000 \text{ s/mm}^2$ ) are acquired, which attenuates most of the fast-diffusing water. The proposed preparation module has the disadvantage of measuring only 25% of the available signal. First, 50% of the available signal is lost due to the stimulated echo preparation; and second, an additional 50% of the signal is lost due to the magnitude stabilizing gradients. Despite the inherently low SNR, the developed

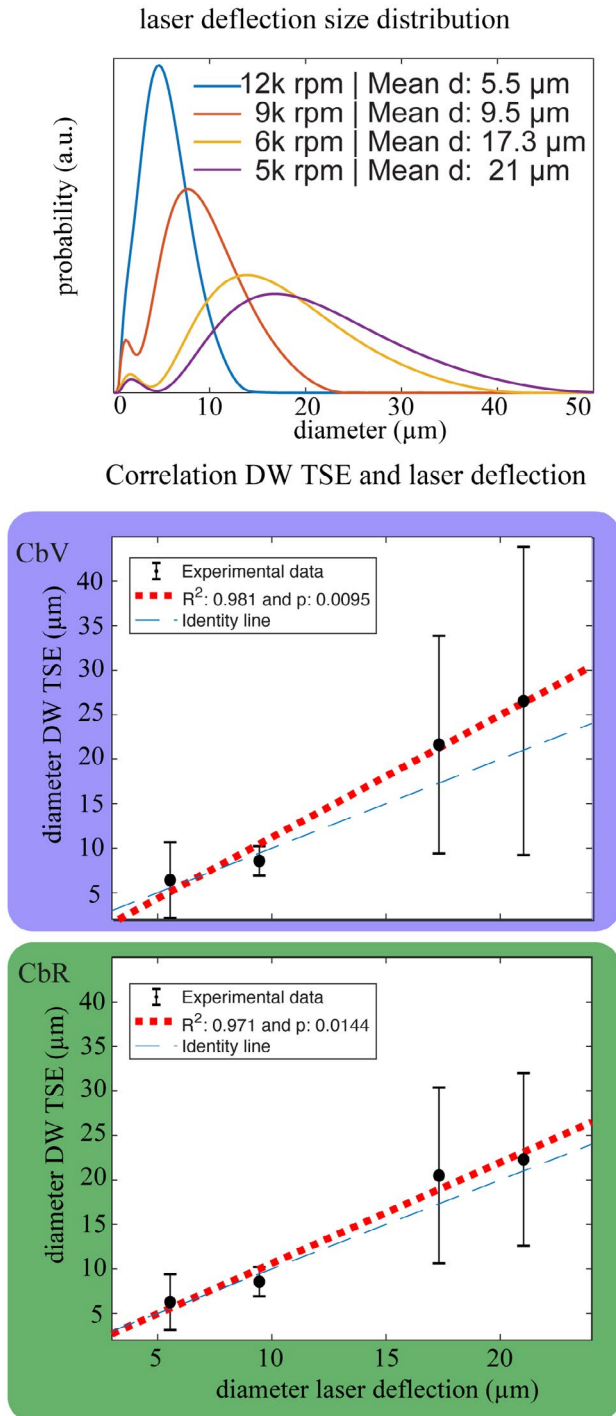


**FIGURE 7** Correlation analysis of the droplet diameter results obtained with DW MRI compared with the laser-deflection measurement. The laser-deflection measurements revealed an increasing lipid droplet size and distribution broadness with decreasing frequency of the colloid mill. Both presented processing methods (CbV and CbR) correlate significantly with the reference-method laser deflection ( $R^2 > 0.95$  and  $P < 5\%$ ). With the CbV processing, the linear fit deviates from the identity line (slope/offset: 1.37/−2.52 μm). With the CbR processing, the linear fit again approaches the identity line (slope/offset: 1.13/−0.71 μm)

technique enables very strong DW with reduced sensitivity to motion-induced phase errors (single-shot TSE design using magnitude stabilizers) and off-resonance effects (TSE design), and allows the acquisition of DW data at varying diffusion times (STE preparation). To sensitize the acquired signal to diffusion restriction effects, longer diffusion times and higher b-values would increase the sensitivity of the measurement to lipid diffusion restriction effects. However, longer diffusion times or higher b-values would increase the required preparation's TE and TM, and are therefore not easily realizable because they would further reduce the measurement SNR.

The present work shows that the lipid droplet-size fitting is challenging, especially for estimating larger diameters. When the DW signal decay curves are compared, different parameter combinations result in very similar decay curves, even without noise (Figure 3). Specifically, small residual variations were observed within a large region around the reference diameter and diffusion coefficient. This might not be critical for smaller diameters, because the lipid droplet diameter can be precisely determined. With increasing size, the curvature and the extent of the region with small residual variation increases, resulting in underestimated and overestimated diameters with very similar DW signal decays.

With added noise, certain parameter combinations within the minimum valley can form local minima. The fitting problem becomes ill-posed and cannot be solved with a standard approach. Using multiple starting values for the fitting process is recommended to find the global, and not only a local, minimum. However, with low SNR, even the approach with multiple starting values can fail, as observed in the noise simulations (Figures 4 and 5). In a 2D histogram of the diameter and corresponding free diffusion constant estimates, similarities to the minimum valleys in Figure 3 can be observed. Because of the small gradient within the minimum valley, a stopping of the fitting within the minimum valley is likely, especially with noisy signals.

When investigating the simulated mean diameter in the phantom case, only deviations from the true value are observed for the minimal SNR with smaller SD with the CbR processing compared with MbV and CbV. With increasing  $SNR_{\text{effective}}$ , all three processing methods approach the true diameter with a small SD. Due to the rather strong restriction effects and high  $SNR_0$  in this phantom scenario, the results from MbV and CbV are similar, whereas the CbR processing shows the same trend but smaller bias and SD. In the simulated AT sample case, much broader droplet diameter and free diffusion-estimate distributions are observed. This can be explained by the small diffusion-restriction effects in the AT samples. The SD in diameter estimation decreases with increasing  $SNR_{\text{effective}}$ . A large underestimation bias is observed, even at high  $SNR_{\text{effective}}$ , with the MbV processing.

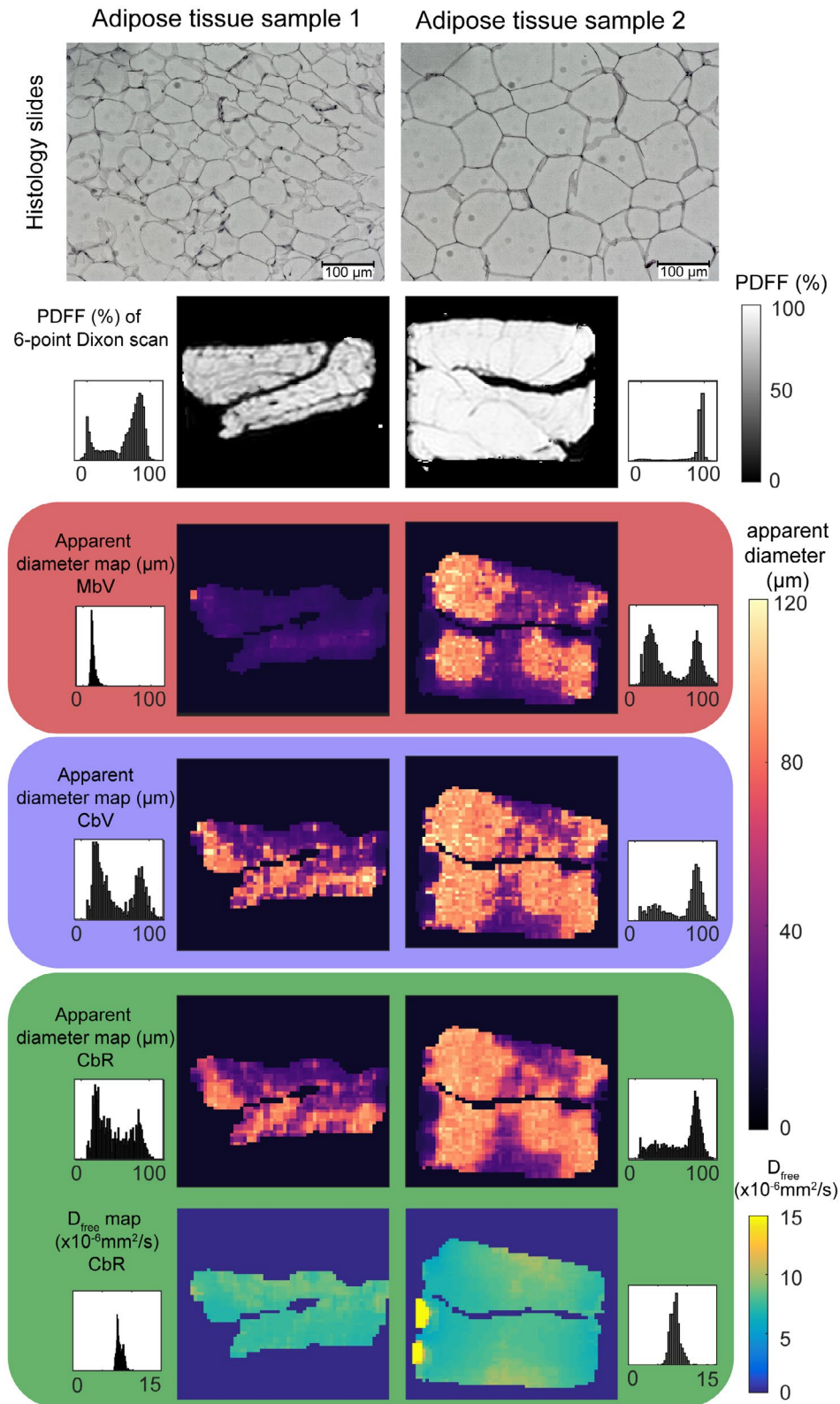


**FIGURE 8** Histology slides, proton density fat fraction (PDFF) maps, MbV-based, CbV-based and CbR-based apparent diameter maps, CbR-based free diffusion constant, and corresponding histograms for two AT samples. Adipose-tissue sample 1 shows larger heterogeneity in the PDFF compared with AT sample 2, and a smaller mean adipocyte size in the histology. The apparent diameter map obtained by MbV processing yields very low apparent-diameter estimates in the low-SNR sample compared with the high-SNR sample. When the apparent lipid droplet size is estimated with the CbV processing, larger droplet diameters are extracted in both samples. The SD is decreased with the CbR compared to the CbV processing (broadness in the diameter histograms). The free diffusion constant maps give similar values in both samples

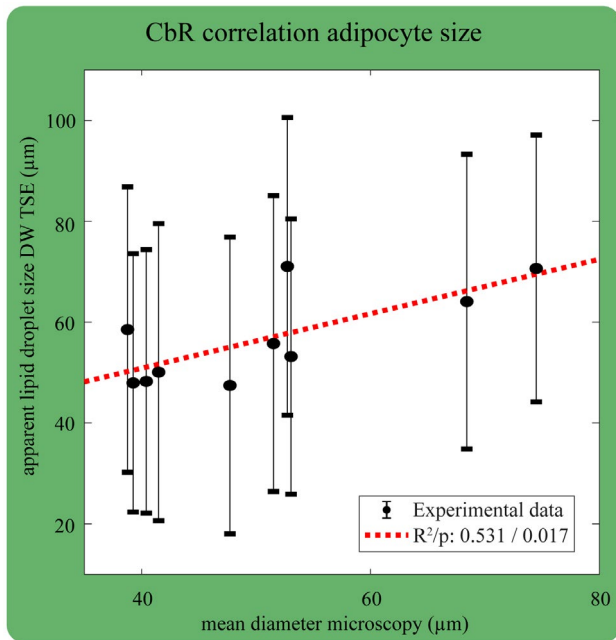


**FIGURE 9** Correlation analysis of the mean apparent droplet diameter obtained with CbR processing compared with microscopy in AT sample study. A significant correlation was found when comparing the mean lipid droplet size ( $R^2/P$ : 0.531/0.017) obtained by both methods, although a large uncertainty was found in the size estimation of the MR-based method. Mean values  $\pm 1$  SD (error bar) are shown

Magnitude averaging can lead to a noise floor, which decreases the measured ADC at longer diffusion times, corresponding to a signal behavior that is characteristic for smaller droplet sizes. With complex averaging, noise bias effects are reduced and the true diameter is only slightly overestimated. The CbR processing not only reduces the SD but also eliminates the bias. The noise simulation reveals that an accurate estimation of large lipid droplet diameters is feasible when the  $SNR_{\text{effective}}$  is high enough and the data are complex-averaged. The proposed CbR processing yields more accurate and precise results compared with the other two studied fitting approaches.

In the water–fat emulsion phantoms consisting of small lipid droplets, a decreasing ADC curve with increasing diffusion time is observed, which is a clear indicator of diffusion-restriction effects. In coconut oil, no such restriction barriers exist; therefore, the ADC values do not depend on the diffusion time (Supporting Information Figure S2). This analysis can be interpreted as a proof-of-principle experiment, showing the applicability of the presented method to investigate restriction effects of diffusing lipids.

Rather homogenous lipid droplet diameter maps are obtained in phantoms with all processing approaches (Figure 6). The MbV and CbV lead to similar results but show regions with unreasonably large diameters. When the CbR processing is used, the diameter map homogeneity is increased. When comparing the lipid droplet–diameter results from

DW-MRI with laser deflection measurement, a high correlation is found. The diameter maps obtained by CbV included voxel-wise diameter overestimations; therefore, the agreement with laser deflection deviates from the identity line. With the CbV processing, local quantification errors in the droplet-diameter estimates can occur, which can be partly recovered by the proposed CbR processing, leading to a better agreement with the reference method. It can be summarized that the presented methodology provides accurate results in water–fat emulsions (lipid droplet diameter up to 25  $\mu\text{m}$ ).

Measuring the apparent droplet size in AT samples *ex vivo* is challenging because of the small measurable restriction effects due to large droplets and the low lipid diffusivity at room temperature. The two AT samples shown in Figure 8 deviate significantly in their microstructure, as highlighted in the histology images and proton density fat fraction maps. The MbV processing yields too small apparent lipid droplet-size estimates, especially in the low SNR sample. When the CbV processing is used, two distinct apparent diameter peaks are observed in both samples (in agreement with the simulation). When the CbR processing is used, the obtained apparent droplet-diameter map appears smoother and the SD of the apparent diameter estimates is reduced. Within both samples a spatial variation of the apparent diameter map can be observed for all processing approaches. It is unclear whether the observed spatial variation is caused by measurement uncertainties (as indicated in Figure 5) or due to real spatial adipocyte size variations. Given that the used histology provides only a localized estimate of the adipocyte size from the biopsy site, the mean MR-derived apparent droplet diameter (averaged over the acquired 2D slice) was used in the comparison with histology (shown in Figure 9). In the group analysis, a large SD is visible in MRI-based apparent droplet size. Overall, a significant correlation can be observed between the MR-based mean apparent lipid droplet size (with CbR processing) and histology. The results acquired in human AT samples show that it is feasible to estimate an apparent lipid droplet size of *ex vivo* AT and that a similar trend as histology can be observed when examining samples with different mean adipocyte sizes.

An MR-based white adipocyte size estimate could potentially serve as a biomarker for the risk of cardiometabolic diseases and could replace invasive biopsy measurement. Therefore, the proposed technique should be thoroughly validated *ex vivo* with more AT samples, and the *in vivo* application should be subsequently targeted. However, additional significant challenges related to motion and prolonged scan times have to be addressed when measuring *in vivo*.

The described methodology has limitations: First, the measured DW signal is the sum over several fat peaks that have different  $T_1$  relaxation times and potentially different diffusion constants. This is not incorporated in the modeling, which assumes a single component. Because most of the

signal should be associated with the main fat peak, the contribution of these spins should be dominant. Second, the used modeling does not incorporate an underlying cell-size distribution. An asymmetric or multimodal particle-size distribution could induce a bias on the estimated mean adipocyte size, leading eventually to an overestimation or underestimation. Incorporating the estimation of the size distribution in the fitting process can be considered as very challenging because it would require the acquisition of DW data at different diffusion encodings with higher SNR. In addition, a parameterization of the size distribution would need to be known, for which currently no consensus can be found in the literature.<sup>4</sup> However, previous work showed that the broadness of a symmetric particle distribution has minor influence on the mean droplet-size estimation.<sup>11</sup> Third, a partially smooth spatial variation of the lipid droplet size is assumed. Given the fact that subcutaneous fat biopsies are very homogenous and no spatial variation is visible on MR images, the assumption of a slowly varying droplet diameter might be justifiable. Fourth, the balancing term  $\lambda$  is not optimized further, but is instead chosen based on the SNR of the acquired data. Optimizing  $\lambda$  could further reduce quantification errors and should be discussed in further research. Fifth, different existing methods to obtain the adipocyte size from ex vivo AT samples yield different quantitative results.<sup>4</sup> However, this work does not intend to show a quantitative comparison in the AT samples, but rather to demonstrate the feasibility of the developed methodology for large lipid droplet sizes. Sixth, this work is based on a limited sample size in the phantom and the AT study, and includes no optimization of the experimental parameters. Studies using larger sample sizes and further optimizing the experimental parameters are required.

## 5 | CONCLUSIONS

The present work proposes a methodology to probe diffusion restriction effects in lipid droplets in phantoms and ex vivo AT samples at a 3T clinical scanner using a long diffusion time and high b-value DW-TSE sequence. The challenges in estimating the lipid droplet size from DWI data were evaluated with simulations, and strategies to improve the measurement were proposed. Namely, increasing the SNR by complex spatial averaging, using multiple initial fitting starting values, and applying the additional graph-cut postprocessing steps improved both accuracy and precision in estimating lipid droplet size in phantoms and enabled the estimation of an apparent lipid droplet size in ex vivo AT samples. The presented method showed excellent agreement in measuring lipid droplet size against laser deflection in water-fat phantoms and a correlation when the MR-based mean apparent lipid droplet size was compared with histology in ex vivo human AT samples.

## ACKNOWLEDGMENT

The authors thank Oliver Gmach and the chair of Chair for Food and Bioprocess Engineering for the preparation and measurement of the water-fat emulsion phantoms, and Prof. Burgkart for the wooden support table. The authors also thank Stefanie Winkler for assisting with the AT sample collection; Cora Held, Lisa Patzelt, and Mark Zamskiy for assisting with AT sample measurements; and Mingming Wu for the fruitful discussion and the code base for this work.

## DATA AVAILABILITY STATEMENT

Parts of the *MATLAB* code of our implementation of the proposed method will be made freely available for download at [https://github.com/BMRRgroup/DropletSize\\_MurdayCotts](https://github.com/BMRRgroup/DropletSize_MurdayCotts).

## ORCID

Dominik Weidlich  <https://orcid.org/0000-0001-7842-2682>

Julius Honecker  <https://orcid.org/0000-0002-1592-7023>

Christof Boehm  <https://orcid.org/0000-0003-1321-5804>

Stefan Ruschke  <https://orcid.org/0000-0001-9658-6541>

Melina Claussnitzer  <https://orcid.org/0000-0003-2450-736X>

Hans Hauner  <https://orcid.org/0000-0002-1682-5088>

Dimitrios C. Karampinos  <https://orcid.org/0000-0003-4922-3662>

## REFERENCES

- Spalding KL, Arner E, Westermark PO, et al. Dynamics of fat cell turnover in humans. *Nature*. 2008;453:783-787.
- Salans LB, Cushman SW, Weismann RE. Studies of human adipose tissue. Adipose cell size and number in nonobese and obese patients. *J Clin Invest*. 1973;52:929-941.
- Laforest S, Labrecque J, Michaud A, Cianflone K, Tchernof A. Adipocyte size as a determinant of metabolic disease and adipose tissue dysfunction. *Crit Rev Clin Lab Sci*. 2015;52:301-313.
- Laforest S, Michaud A, Paris G, et al. Comparative analysis of three human adipocyte size measurement methods and their relevance for cardiometabolic risk. *Obesity*. 2017;25:122-131.
- Assaf Y, Blumenfeld-Katzir T, Yovel Y, Basser PJ. AxCaliber: a method for measuring axon diameter distribution from diffusion MRI. *Magn Reson Med*. 2008;59:1347-1354.
- Lehnert A, Machann J, Helms G, Claussen CD, Schick F. Diffusion characteristics of large molecules assessed by proton MRS on a whole-body MR system. *Magn Reson Imaging*. 2004;22:39-46.
- Steidle G, Eibofner F, Schick F. Quantitative diffusion imaging of adipose tissue in the human lower leg at 1.5 T. *Magn Reson Med*. 2011;65:1119-1125.
- Jezzard P, Barnett AS, Pierpaoli C. Characterization of and correction for eddy current artifacts in echo planar diffusion imaging. *Magn Reson Med*. 1998;39:801-812.
- Anderson AW, Gore JC. Analysis and correction of motion artifacts in diffusion weighted imaging. *Magn Reson Med*. 1994;32:379-387.
- Weidlich D, Zamskiy M, Maeder M, Ruschke S, Marburg S, Karampinos DC. Reduction of vibration-induced signal loss by

- matching mechanical vibrational states: application in high b-value diffusion-weighted MRS. *Magn Reson Med.* 2020;84:39-51.
11. Weidlich D, Honecker J, Gmach O, et al. Measuring large lipid droplet sizes by probing restricted lipid diffusion effects with diffusion-weighted MRS at 3T. *Magn Reson Med.* 2019;81:3427-3439.
  12. Nicolay K, Braun KP, Graaf RA, Dijkhuizen RM, Kruiskamp MJ. Diffusion NMR spectroscopy. *NMR Biomed.* 2001;14:94-111.
  13. Ronen I, Valette J. Diffusion-weighted magnetic resonance spectroscopy. *eMagRes.* 2015;4:733-750.
  14. Brandejsky V, Kreis R, Boesch C. Restricted or severely hindered diffusion of intramyocellular lipids in human skeletal muscle shown by in vivo proton MR spectroscopy. *Magn Reson Med.* 2012;67:310-316.
  15. Cao P, Fan SJ, Wang AM, et al. Diffusion magnetic resonance monitors intramyocellular lipid droplet size in vivo. *Magn Reson Med.* 2015;73:59-69.
  16. Verma SK, Nagashima K, Yaligar J, et al. Differentiating brown and white adipose tissues by high-resolution diffusion NMR spectroscopy. *J Lipid Res.* 2017;58:289-298.
  17. Le Bihan D, Poupon C, Amadon A, Lethimonnier F. Artifacts and pitfalls in diffusion MRI. *J Magn Reson Imaging.* 2006;24:478-488.
  18. Alsop DC. Phase insensitive preparation of single-shot RARE: application to diffusion imaging in humans. *Magn Reson Med.* 1997;38:527-533.
  19. Gmach O, Bertsch A, Bilke-Krause C, Kulozik U. Impact of oil type and pH value on oil-in-water emulsions stabilized by egg yolk granules. *Colloids Surf A Physicochem Eng Asp.* 2019;581:123788.
  20. Tycko R, Cho HM, Schneider E, Pines A. Composite pulses without phase distortion. *J Magn Reson.* 1985;61:90-101.
  21. Van AT, Cervantes B, Kooijman H, Karampinos DC. Analysis of phase error effects in multishot diffusion-prepared turbo spin echo imaging. *Quant Imaging Med Surg.* 2017;7:238-250.
  22. Pipe JG. Motion correction with PROPELLER MRI: application to head motion and free-breathing cardiac imaging. *Magn Reson Med.* 1999;42:963-969.
  23. Murday JS, Cotts RM. Self-diffusion coefficient of liquid lithium. *J Chem Phys.* 1968;48:4938-5000.
  24. Cui C, Wu X, Newell JD, Jacob M. Fat water decomposition using globally optimal surface estimation (GOOSE) algorithm. *Magn Reson Med.* 2015;73:1289-1299.
  25. Boehm C, Diefenbach MN, Makowski MR, Karampinos DC. Improved body quantitative susceptibility mapping by using a variable-layer single-min-cut graph-cut for field-mapping. *Magn Reson Med.* 2021;85:1697-1712.
  26. Shah A, Abámoff MD, Wu X. Optimal surface segmentation with convex priors in irregularly sampled space. *Med Image Anal.* 2019;54:63-75.
  27. Engl HWH, Neubauer MA. *Regularization of Inverse Problems.* Dordrecht, Netherlands: Springer; 2000. p 322.
  28. Guilmineau F, Kulozik U. Influence of a thermal treatment on the functionality of hen's egg yolk in mayonnaise. *J Food Eng.* 2007;78:648-654.
  29. Eggers H, Brendel B, Duijndam A, Herigault G. Dual-echo Dixon imaging with flexible choice of echo times. *Magn Reson Med.* 2011;65:96-107.

## SUPPORTING INFORMATION

Additional Supporting Information may be found online in the Supporting Information section.

**FIGURE S1** Simulated longitudinal magnetization after preparation for a stimulated echo preparation with 90° hard pulses (left) and 90° MLEV scheme pulses. With MLEV scheme 90° a larger insensitivity towards frequency offsets can be observed

**FIGURE S2** Diffusion signal decay curves at increasing diffusion times (different columns) for the water-fat emulsion phantoms and the coconut oil (different rows). At each diffusion time and the investigated phantom, the signal decay is mono-exponential. In the water-fat-emulsions a clear ADC decay is visible for increasing diffusion time, whereas such a trend is not visible in the coconut oil

**How to cite this article:** Weidlich D, Honecker J, Boehm C, et al. Lipid droplet-size mapping in human adipose tissue using a clinical 3T system. *Magn Reson Med.* 2021;86:1256–1270. <https://doi.org/10.1002/mrm.28755>